

RELATIONS BETWEEN THE SIZES OF GALAXIES AND THEIR DARK-MATTER HALOS AT REDSHIFTS $0 < z < 3$ KUANG-HAN HUANG¹, S. MICHAEL FALL², HENRY C. FERGUSON², ARJEN VAN DER WEL³, NORMAN GROGIN², ANTON KOEKEMOER², SEONG-KOOK LEE⁴, PABLO G. PÉREZ-GONZÁLEZ⁵, AND STIJN WUYTS⁶

Draft version December 3, 2024

ABSTRACT

We derive relations between the effective radii R_{eff} of galaxies and the virial radii R_{200c} of their dark-matter halos over the redshift range $0 < z < 3$. For galaxies, we use the measured sizes from deep images taken with *Hubble Space Telescope* for the CANDELS program; for halos, we use the inferred sizes from abundance matching to cosmological dark-matter simulations via a stellar mass–halo mass (SMHM) relation. For this purpose, we derive a new SMHM relation based on the same selection criteria and other assumptions as for our sample of galaxies with size measurements. As a check on the robustness of our results, we also derive $R_{\text{eff}}-R_{200c}$ relations for three independent SMHM relations from the literature. We find that galaxy R_{eff} is proportional on average to halo R_{200c} , confirming and extending to high redshifts the $z = 0$ results of Kravtsov (2013). Late-type galaxies (with low Sérsic index and high specific star formation rate, sSFR) follow a linear $R_{\text{eff}}-R_{200c}$ relation, with effective sizes at $1 < z < 3$ close to those predicted by simple models of disk formation; at $0 < z < 1$, the sizes of late-type galaxies are slightly (~ 0.2 dex) below this prediction. Early-type galaxies (with high Sérsic index and low sSFR) follow a roughly parallel $R_{\text{eff}}-R_{200c}$ relation, $\sim 0.2-0.3$ dex below the one for late-type galaxies. Our observational results, reinforced by recent hydrodynamical simulations, indicate that galaxies grow quasi-homologously with their dark-matter halos.

Subject headings: galaxies: evolution — galaxies: high-redshift — galaxies: structure — methods: data analysis

1. INTRODUCTION

The size of a galaxy, as measured by its half-mass radius R for example, is among the most basic of its properties. Together with the mass M , the size R determines the binding energy, $E \approx GM^2/(2R)$, and hence the energy radiated away during the formation of the galaxy. For galactic disks, with stars and gas on nearly circular orbits with rotation velocity V_{rot} , the size R is determined by the angular momentum $J \approx MRV_{\text{rot}}$, which in turn determines the energy $E = \frac{1}{2}MV_{\text{rot}}^2 \approx G^2M^5/(2J^2)$. The basic description of galaxies in general consists of M , R , and V_{rot} , or equivalently M , E , and J , while for disk-dominated galaxies, any two of these quantities suffice.

As a result of the hierarchical growth of galaxies, we expect their masses and radii to increase with cosmic time and thus to decrease with redshift. In the simplest models of galaxy formation, the sizes of the baryonic components of galaxies are, on average, proportional to the sizes of their surrounding dark-matter halos. For galactic disks, this proportionality in sizes follows directly from the assumed proportionality of the angular momentum of baryons and dark matter resulting from tidal torques in the early stages of galaxy formation (Fall & Efstathiou 1980; Mo et al. 1998). This assumption underlies

all of the many semi-analytical models of galaxy formation in current use (e.g., Cole et al. 2000; Croton et al. 2016). Recent hydrodynamical simulations of galaxy formation confirm the approximate proportionality between the angular momentum of galaxies and their dark-matter halos (Genel et al. 2015; Pedrosa & Tissera 2015; Teklu et al. 2015; Zavala et al. 2016).

There have been numerous searches for the expected decrease in galactic sizes with redshift based on measurements of deep images taken with the *Hubble Space Telescope* (*HST*) over the past dozen years (e.g., Ferguson et al. 2004; Hathi et al. 2008; Mosleh et al. 2012). These searches all find that galaxies were smaller in the past, by roughly the predicted amount, although there are significant differences in the precise decline of galactic sizes with redshift among these studies (compare e.g. Shibuya et al. 2015 and Curtis-Lake et al. 2016). Part of the discrepancy among these results stems from the fact that the apparent evolution in sizes depends on how galaxies at different redshifts are compared, whether at fixed stellar mass or luminosity or at variable stellar mass or luminosity.

Kravtsov (2013) used stellar-mass–halo-mass (SMHM) relations derived via the technique of abundance matching to compare the observed sizes of present-day galaxies with the sizes of their matched dark-matter halos in cosmological N -body simulations. He found that the sizes of galaxies at $z = 0$ are proportional on average to the sizes of their halos. Furthermore, the coefficient of proportionality is consistent with a simple model in which galactic disks grow with approximately the same specific angular momentum as their halos until $z \sim 2$ and then stop growing after that. The question immediately arises whether the same or a different relation holds between the sizes of galaxies and their halos at high redshifts. The purpose of this paper is to answer this question.

The advantage of comparing the sizes of galaxies at multiple redshifts with the sizes of their matched halos at the same

E-mail: khhuang@ucdavis.edu

¹ University of California Davis, 1 Shields Avenue, Davis, CA 95616, USA; khhuang@ucdavis.edu² Space Telescope Science Institute, 3700 San Martin Drive, Baltimore, MD 21218, USA³ Max Planck Institute for Astronomy, Königstuhl 17, D-69117 Heidelberg, Germany⁴ Center for the Exploration of the Origin of the Universe, Department of Physics and Astronomy, Seoul National University, Seoul, Korea⁵ Departamento de Astrofísica, Facultad de CC. Física, Universidad Complutense de Madrid, E-28040, Madrid, Spain⁶ Department of Physics, University of Bath, Claverton Down, Bath, BA2 7AY, UK

TABLE 1
GALAXY SAMPLE SIZES

Redshift	Wide	Deep	HUDF	Total	z_{med}	$M_{*,\text{low}}^a$ (M_{\odot})
$0.0 < z < 0.5$	4388	923	50	5361	0.34	1.0×10^7
$0.5 < z < 1.0$	9706	2435	116	12257	0.73	5.0×10^7
$1.0 < z < 1.5$	6666	1395	113	8174	1.23	8.2×10^7
$1.5 < z < 2.0$	5152	1224	90	6466	1.70	1.7×10^8
$2.0 < z < 2.5$	2580	727	47	3354	2.23	2.1×10^8
$2.5 < z < 3.0$	1483	497	54	2034	2.69	3.8×10^8
All Redshifts	29975	7201	470	37646

^a Typical stellar mass of the galaxies from HUDF with $26.6 < H_{160} < 26.8$ and near the median of each redshift bin. In the lowest redshift bin, we impose a hard cut in stellar mass at $10^7 M_{\odot}$.

redshifts, as we do here, is that the results are then expressed directly in simple, physically meaningful terms. In fact, virtually all predictions of galaxy sizes at high redshifts are based on the assumption that they grow in proportion to halo sizes.

There are already a couple of indications that the sizes of galaxies and their halos evolve in lockstep. First, semi-empirical models of galaxy formation that make this assumption agree better with deep *HST* images than the same models with different assumptions about the evolution of galactic sizes (Taghizadeh-Popp et al. 2015). Second, recent measurements of the sizes and rotation velocities of galactic disks at $1 < z < 3$ and $0.2 < z < 1.4$ indicate that they have approximately the same angular momenta as their dark-matter halos (Burkert et al. 2016; Contini et al. 2016). While these results are suggestive, it is still important to make a direct, independent comparison of the sizes of high-redshift galaxies with the sizes of their matched halos, the investigation we describe here.

The plan for the remainder of this paper is the following. In Section 2, we describe our sample of galaxies and measurements of their sizes and other properties. In Section 3, we discuss the abundance matching method and its implementation with four different stellar mass–halo mass (SMHM) relations. In Section 4, we present the results of our comparison of galaxy and halo sizes, and in Section 5, we discuss the uncertainties in these results. We discuss some implications of our results in Section 6 and demonstrate the transformation from galaxy size–stellar mass relations in Appendix 6. All magnitudes quoted in this paper are in the AB system, and we assume the following cosmological parameters: $h = 0.7$, $\Omega_m = 0.27$, and $\Omega_{\Lambda} = 0.73$.

2. GALAXY SAMPLE AND MEASUREMENTS

For this study, we need a galaxy sample with homogeneous data quality that enables accurate size measurements. *HST* images are required because galaxies at $z > 1$ are generally smaller than $1''$. We also need a galaxy sample with good constraints on redshifts, stellar masses and star formation rates, so that we can connect galaxies to dark-matter halos and distinguish star forming galaxies from quiescent galaxies. The Cosmic Assembly Near-infrared Deep Extragalactic Legacy Survey (CANDELS) is the best data set currently available for this study: all five CANDELS fields, covering $\approx 800 \text{ arcmin}^2$ in total, have *HST* images at optical and near-IR wavelengths with uniform quality (Grogin et al. 2011; Koekemoer et al. 2011). The high angular resolution of *HST* ($\lesssim 0''.15$ in the near-IR) is able to resolve most galaxies at $z \leq 3$. In addition, ancillary spectroscopic and imaging data combine with *HST* data to provide tight constraints on galaxy redshifts, stellar

masses, and star formation rates. CANDELS has three tiers of depth. The Wide region covers $\sim 675 \text{ arcmin}^2$ to a 5σ limiting magnitude $H_{160} \sim 27.3 \text{ mag}$ in a $0.17''$ aperture. The Deep region covers $\sim 125 \text{ arcmin}^2$ to $H_{160} \sim 28.1 \text{ mag}$. The survey also encompasses the Hubble Ultra-Deep Field (HUDF)—the HUDF09 (Bouwens et al. 2010) program and HUDF12 (Ellis et al. 2013 and Koekemoer et al. 2013; see also Illingworth et al. 2013) covers $\sim 5 \text{ arcmin}^2$ —to $H_{160} \sim 29.7 \text{ mag}$.

We take the photometry, spectroscopic and photometric redshifts, and stellar-mass estimates from the CANDELS-team catalogs (Guo et al. 2013; Galametz et al. 2013; Santini et al. 2015; Nayyeri et al. 2016, Stefanon et al. 2016, Barro et al., in prep.). The size estimates are taken from van der Wel et al. (2012).

We select all galaxies at $0 < z < 3$ in the CANDELS fields for this study. We cap our galaxy redshifts at $z = 3$ because this is the highest redshift where *HST* still samples redward of rest-frame 4000\AA , and at $z > 3$ surface-brightness selection effects start to significantly impact galaxy samples detected in *HST* images (Taghizadeh-Popp et al. 2015). Sources are detected using SExtractor (Bertin & Arnouts 1996) in H_{160} . Roughly 10% of these sources have high quality spectroscopic redshifts, which are used in calibrating the photometric redshifts for the remaining sources.

Galaxy sizes are measured in H_{160} and J_{125} by fitting a single Sérsic profile to each galaxy using GALFIT (Peng et al. 2010). We define galaxy sizes as effective radii (R_{eff}) along the major axis, the radii within which Sérsic profiles contain half of the total integrated light. We discuss the de-projection from 2D to 3D later when comparing with theoretical expectations. Our overall sample is dominated by late-type galaxies at all redshifts, whose disk components have the same 2D and 3D half-light radii.

Using simulations with artificial galaxies and comparisons of measurements in different imaging depths, van der Wel et al. (2012) concluded that down to $H_{160} = 24.5 \text{ mag}$ in the CANDELS Wide region, the systematic (random) errors of R_{eff} measurements are below $\sim 20\%$ (30%). Meanwhile, the systematic (random) errors of Sérsic index n measurements are below $\sim 50\%$ (60%). The quoted errors here are for galaxies with $n > 3$, which tend to have larger errors than galaxies with $n < 3$. Therefore, we select all galaxies down to $H_{160} = 24.5 \text{ mag}$ in the CANDELS Wide region, $H_{160} = 25.2 \text{ mag}$ in the Deep region, and $H_{160} = 26.7 \text{ mag}$ in the HUDF. These magnitude limits correspond to similar S/N limits.

In addition to magnitude cuts, we prune the sample as follows. We reject all sources that have problematic photometry (generally those at the borders of the image or falling on stellar diffraction spikes). We eliminate sources that are identified as AGNs via X-ray or IR SEDs. We discard as point sources all objects that have half-light radii (measured by SExtractor) smaller than 2.6 pixels. We enforce the following criteria to eliminate galaxies with poor GALFIT fits: (1) the GALFIT measurement is flagged as poor in the catalogs from van der Wel et al. (2012); (2) the error in the measured R_{eff} exceeds $0.3R_{\text{eff}}$; (3) the measured n lies outside the range $0.1 < n < 8$, which usually signals problematic fits. The GALFIT, AGN, and point-source criteria combined reject roughly $1/4$ of the sources that satisfy the magnitude cuts. The number of sources that pass all the cuts above are listed in Table 1.

The existence of the very deep HUDF data allows us to test whether selection effects, measurement biases, or the pruned

ing procedure are biasing our samples near their faint limits. In Figure 1 (top panels), we compare the size distributions in the Wide region and the HUDF for the magnitude range $23.5 < H_{160} < 24.5$ before and after pruning, finding no significant difference. If the HUDF were picking up many more low-surface brightness objects, we would have expected to see that show up in the tail of the distribution. Instead we see more large-radius objects in the Wide sample, most of which are pruned away as bad fits, but without having much impact on the median R_{eff} . A Kolmogorov-Smirnoff test yields p values consistent with the samples being drawn from the same underlying distribution. Figure 1 shows the same comparison for the Deep region in the magnitude range $24.2 < H_{160} < 25.2$ mag. We made a similar comparison for the stellar mass distributions, also finding no statistically significant difference between the HUDF and the Deep and Wide samples. The surface brightness detection limits were also presented in Guo et al. (2013) for GOODS-S (see their Figure 5). At our magnitude limits, we are 90% complete for galaxies smaller than $\approx 0.24''$ in Wide, $\approx 0.27''$ in Deep, and $\approx 0.12''$ in HUDF. Figure 1 shows that the majority of galaxies in our sample are smaller than these limits, so surface brightness detection completeness is not an issue.

Studying galaxy size evolution demands that we compare R_{eff} values at a similar rest-frame wavelength across redshift bins, so that we can eliminate the contributions from dust or stellar age gradient to the observed size evolution. We follow the procedure in van der Wel et al. (2014) to correct for galaxy color gradients and place galaxy sizes on the same rest-frame wavelength. To do this, we use galaxy sizes measured in H_{160} for galaxies at $z > 1.5$ and use the sizes measured in J_{125} at $z < 1.5$. Color gradients that lead to different galaxy sizes at different wavelengths are accounted for by a correction factor that is a function of galaxy redshift, stellar mass, and galaxy type (late-type or early-type). As the result of this color gradient correction, the measurements are converted into the R_{eff} near rest-frame 5000Å. The size correction is typically only a few per cent, but it does reach $\sim 60\%$ in some cases. For more details about the color gradient correction, we refer the readers to van der Wel et al. (2014), Section 2.2, and their equations (1) and (2).

Stellar masses and star formation rates are estimated by comparing our photometry with model spectral energy distributions (SEDs), adopting Chabrier (2003) initial mass function (IMF). Here stellar masses refer to the total mass in stars and stellar remnants at the time of observation, not including the material ejected by stars. This method of estimating stellar masses has been extensively tested in Mobasher et al. (2015), and they found that typical stellar mass uncertainties are ~ 0.25 dex for the magnitude limits adopted here. The primary sources of systematic uncertainties are IMF and stellar evolution models; for galaxies with strong nebular emission lines, systematic uncertainties for stellar mass can be up to ~ 0.4 dex.

We restrict our overall study to galaxies with stellar masses $M > 10^7 M_{\odot}$. Above this limit, we include all galaxies down to the magnitude limits mentioned above, where we are confident that our measurements are robust and unaffected by size-dependent biases. For each redshift interval, we estimate the typical stellar mass of the faintest galaxies by taking the median SED-fitted stellar mass estimate of galaxies within 0.1 mag of the HUDF magnitude limit. The estimated values are listed in Table 1 and shown as vertical tick marks on Figures

5–9. SED-based star formation rates can be uncertain to ~ 0.4 dex (Salmon et al. 2015), therefore the specific star formation rates (sSFR) uncertainties are roughly $\lesssim 0.6$ dex for our galaxy sample. We will only use sSFR to select subsamples in the tails of the sSFR distributions. Because we are making a differential comparison between the relatively large populations in these tails, our results are not sensitive to the sSFR uncertainties.

3. ABUNDANCE MATCHING

In this study, we employ the technique of abundance matching to estimate the mass and thence the size of the dark-matter halo associated with each galaxy in our sample. In essence, this technique compares the measured sizes of observed galaxies with the inferred sizes of matched halos in cosmological dark-matter simulations. The basic assumption is that the rank ordering of galaxy (stellar) masses M_* reflects on average the rank ordering of halo (virial) masses M_{200c} , i.e., that the cumulative number densities of galaxy masses and halo masses are equal: $n_g(> M_*) = n_h(> M_{200c})$. This ansatz leads directly to a correspondence between M_* and M_{200c} known as the stellar mass–halo mass (SMHM) relation. While the assumption that galaxy masses and halo masses follow the same rank ordering is a reasonable approximation for statistical studies based on large samples such as ours, it cannot be exactly true for individual galaxies, which experience stochastic events such as mergers and starbursts throughout their histories.

Given a SMHM relation, we compute the halo mass M_{200c} of each galaxy in our sample from its stellar mass M_* . We then compute the virial halo radius R_{200c} using the standard formula

$$R_{200c} = \left[\frac{3M_{200c}}{4\pi \cdot 200\rho_{\text{crit}}(z)} \right]^{1/3}, \quad (1)$$

where $\rho_{\text{crit}}(z)$ is the critical density of the Universe at redshift z . In order to assess how sensitive our results are to the choice of SMHM relation, we perform all of our calculations with four different SMHM relations. These SMHM relations are each calibrated with a Chabrier (2003) stellar IMF and all converted to the same halo mass definition M_{200c} . They are plotted in Figures 2, 3, and 4 and discussed below.

SMHM relation 1. We have derived this new SMHM relation specifically for this study so that it is as consistent as possible with the CANDELS data set, selection criteria, and SED fitting procedure for our sample of galaxies with size measurements. In particular, we combine the stellar mass function $n_g(> M_*)$ from Tomczak et al. (2014) with our determination of the halo mass function $n_h(> M_{200c})$ from the Millennium-II simulation (Boylan-Kolchin et al. 2009).

Tomczak et al. (2014) derived the stellar mass function of galaxies at $0.2 < z < 3$ in three of the five CANDELS fields, using very similar selection criteria and procedure for estimating stellar masses as those for our sample described in Section 2. We compare our stellar masses with those used by Tomczak et al. (2014)⁷ and find no significant offsets with just a small scatter (~ 0.1 dex). They fitted a double Schechter function to the observed stellar mass function in differential form $dn_g(> M_*)/dM_*$ in each of eight redshift bins. We adopt the Tomczak et al. results directly for the three bins of width $\Delta z = 0.5$ covering the range $1.5 < z < 3.0$. However, for sim-

⁷ These stellar masses are published by the ZFOURGE team (Straatman et al. 2016) and can be downloaded from <http://zf4orge.tamu.edu>.

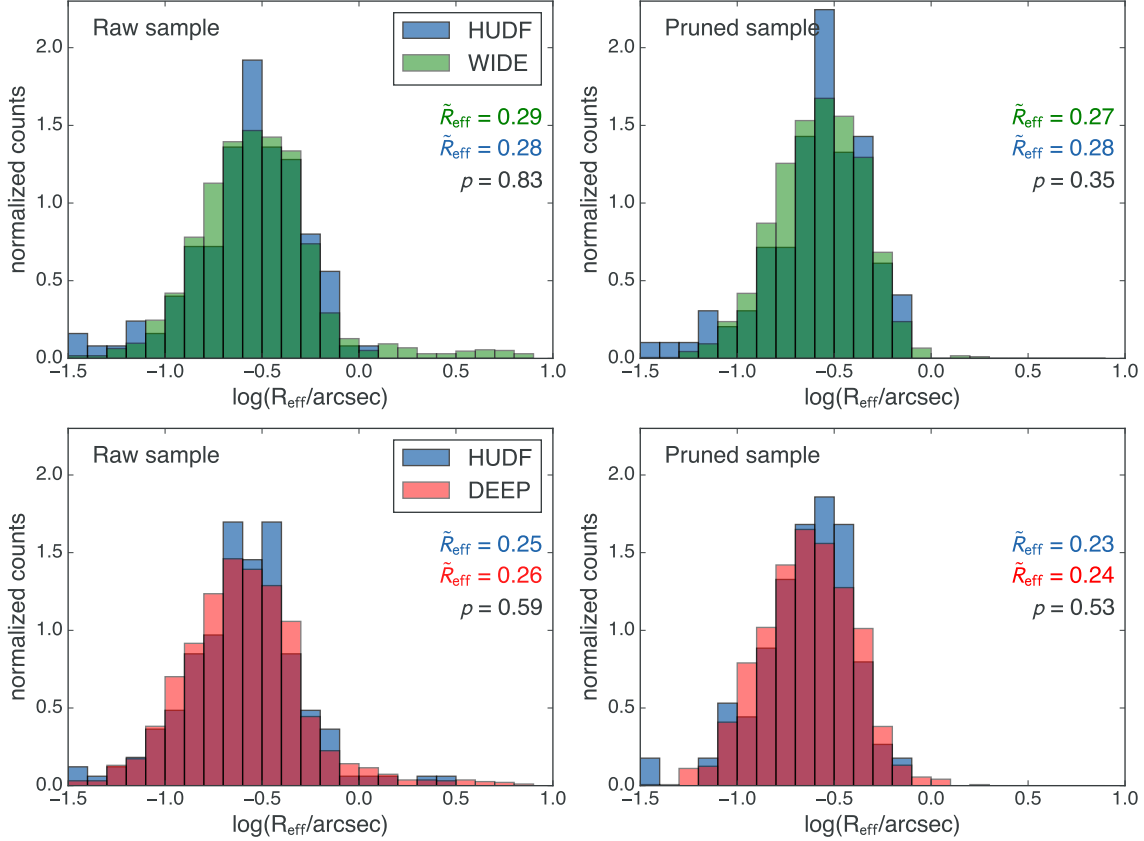


FIG. 1.— Histograms of effective radius R_{eff} for galaxies in narrow magnitude ranges in the Wide, Deep, and HUDF regions of our sample. The top panels compare the distributions of R_{eff} in the Wide and HUDF regions in the magnitude range $23.5 < H_{160} < 24.5$, while the bottom panels compare the distributions of R_{eff} in the Deep and HUDF regions in the magnitude range $24.2 < H_{160} < 25.2$. For reference, the selection limits of our sample in these regions are $H_{160} = 24.5$ (Wide), 25.2 (Deep), and 26.7 (HUDF). The left and right panels compare the distributions before and after the sample pruning described in Section 2. The legends in the panels list the median values of R_{eff} in the four histograms, and the Kolmogorov-Smirnov probabilities that the histograms are drawn from the same underlying distribution. The consistency of the histograms in regions with different depths, before and after pruning, indicates that the distribution of galactic sizes in our sample is unbiased even near the selection limits.

plicity, we combine their results for the four bins of width $\Delta z = 0.25$ covering the range $0.5 < z < 1.5$ into two bins of width $\Delta z = 0.5$. In this step, we weight the observed comoving densities of galaxies by the comoving volume in each $\Delta z = 0.25$ bin and then fit a double Schechter function to the combined comoving densities in each $\Delta z = 0.5$ bin. For our lowest redshift bin, $0 < z < 0.5$, we adopt the Tomczak et al. stellar mass function in their lowest redshift bin, $0.2 < z < 0.5$, because they have shown that this agrees well with the one at $z \approx 0.1$ derived by Moustakas et al. (2013). Finally, we have derived the halo mass function $n_h(> M_{200c})$ from the Millennium-II simulation (Boylan-Kolchin et al. 2009) at the snapshot closest to the middle of each redshift bin and then matched this to the stellar mass function as described above to obtain the SMHM relation.

As a check on this procedure, we have independently derived our own stellar mass function from scratch by the $1/V_{\text{max}}$ method for the galaxies in all five CANDELS fields in the six $\Delta z = 0.5$ bins (albeit with a approximate K -corrections in estimating $1/V_{\text{max}}$). The resulting stellar mass function is nearly identical to the rebinned one from Tomczak et al. (2014). This adds to our confidence in the validity of SMHM relation 1, which we regard as the primary SMHM relation in this study.

Because our galaxy sample covers a wider range in stellar mass than that covered by Tomczak et al. (2014), we linearly extrapolate the SMHM relation in log-log space to both lower

and higher masses beyond the range covered by Tomczak et al. (2014). The solid lines in Figure 2 show the mass range covered by Tomczak et al. (2014), and the dashed lines show the linearly-extrapolated SMHM relation.

SMHM relation 2. Behroozi et al. (2013) derived this SMHM relation from published stellar mass and halo mass functions over a wide range of redshifts ($0 < z < 8$). This is probably the most prevalent SMHM relation in the literature. However, since it is based on stellar mass functions that are quite different from those derived using CANDELS data, it is not ideal for the present study. We use it mainly to gauge the sensitivity of our results to different SMHM relations. For consistency, we convert their halo mass M_{vir} , defined using a redshift-dependent overdensity factor $\Delta_{\text{vir}}(z)$ (Bryan & Norman 1998), to our halo mass definition M_{200c} . The conversion assumes an NFW halo mass profile and the halo mass-concentration model calibrated in Diemer & Kravtsov (2015). The corrections are very small in general (< 0.1 dex).

SMHM relation 3. This is the same SMHM relation adopted by Kravtsov (2013). He derived his own SMHM relation out of concerns that previous relations used stellar mass functions that are biased at both the high-mass and low-mass ends. By using the same SMHM relation as Kravtsov (2013), we can directly compare our galaxy size-halo size relation with his at $z = 0$.

SMHM relation 4. Relations were derived separately for

blue and red central galaxies at $z = 0$ by Rodríguez-Puebla et al. (2015) using abundance matching. We use the blue and red SMHM relations for galaxies with Sérsic index n below and above 2.5, respectively. Several SMHM relations separated by galaxy type exist in the literature at $z < 0.5$, and we compare them in Figure 3. They use different approaches to derive the ratio between stellar masses and halo masses, ranging from abundance matching (Rodríguez-Puebla et al. 2015) to weak lensing (Hudson et al. 2015; Mandelbaum et al. 2016) to a mixture of the two methods (Dutton et al. 2010). We adopt the relation from Rodríguez-Puebla et al. (2015) because it has the largest dynamic range in halo mass, and it is in the middle of the range spanned by all such relations from the literature. Like Behroozi et al. (2013), they also defined their halo mass using $\Delta_{\text{vir}}(z)$, so we apply the same halo mass conversion as we did for SMHM relation 2.

We compare the four SMHM relations in Figure 4. Evidently, there are significant discrepancies among these SMHM relations, especially the first and second, for which the differences can be up to ~ 0.5 dex at $z \sim 3$. Our SMHM relation 1, derived specifically for the CANDELS sample at $0 < z < 3$, shows stronger redshift evolution than SMHM relation 2 from Behroozi et al. (2013). As already noted, this difference comes mainly from the different stellar mass functions used as input to these SMHM relations. Fortunately, as we show in Section 4 and 5, our main scientific results are relatively insensitive to the adopted SMHM relation, largely due to the weak dependence of halo size on halo mass ($R_{200c} \propto M_{200c}^{1/3}$).

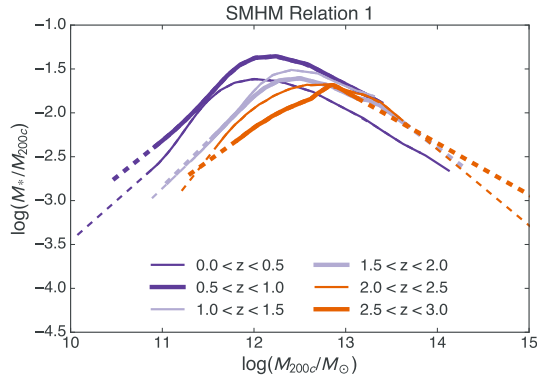


FIG. 2.— Ratio of galaxy stellar mass M_* to halo virial mass M_{200c} plotted against M_{200c} for our primary SMHM relation in six redshift bins covering the range $0 < z < 3$. We derived this SMHM relation by abundance matching from an evolving stellar mass function appropriate for the CANDELS sample (Tomczak et al. 2014) and the evolving halo mass function in the Millennium-II simulation (Boylan-Kolchin et al. 2009) as described in Section 3. Solid lines span the stellar mass ranges of the stellar mass function from Tomczak et al. (2014); we linearly extrapolate the SMHM relation in log-log space to cover the stellar mass range of our sample (dashed lines).

4. RESULTS

The main results of this paper are displayed in Figures 5 to 9 and described in this section. The uncertainties in these results, mostly stemming from the SMHM relation and morphological classification, are discussed in Section 5.

Our first main result is that galaxy sizes are proportional to halo sizes over a wide range of size and mass. Figure 5 shows galaxy R_{eff} plotted against halo R_{200c} at $0 < z < 0.5$ for the four different SMHM relations. In each panel, the medians (16–84 percentile ranges) of $\log R_{\text{eff}}$ in $\log R_{200c}$ bins of

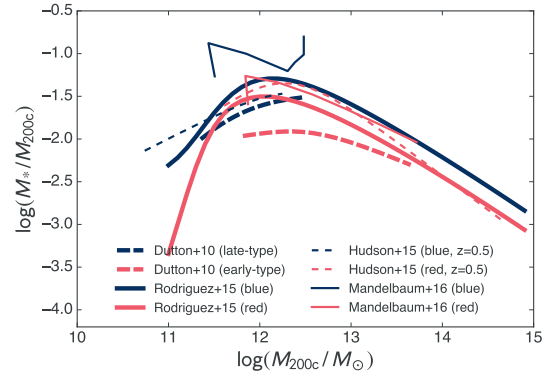


FIG. 3.— Ratio of galaxy stellar mass M_* to halo virial mass M_{200c} plotted against M_{200c} for four low-redshift SMHM relations from the literature that depend on galaxy color or type. These were derived by abundance matching (Rodríguez-Puebla et al. 2015), weak lensing (Hudson et al. 2015; Mandelbaum et al. 2016), or a combination of both techniques (Dutton et al. 2010). Three of the SMHM relations pertain to $z = 0$ and one to $z = 0.5$ (Hudson et al. 2015). Note the large discrepancies among these color- and type-dependent SMHM relations.

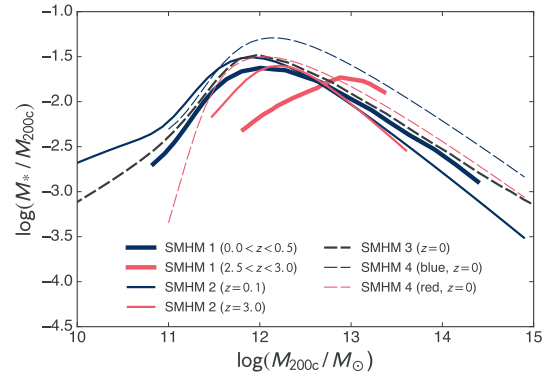


FIG. 4.— Ratio of galaxy stellar mass M_* to halo virial mass M_{200c} plotted against M_{200c} for the four SMHM relations adopted in this work. *SMHM relation 1*: derived as described in Section 3 for all galaxies at $0 < z < 3$ and displayed here at $0 < z < 0.5$ and $2.5 < z < 3.0$, which bracket the relation at intermediate redshifts. *SMHM relation 2*: derived by Behroozi et al. (2013) for all galaxies at $0 < z < 8$ and displayed here at $z = 0.1$ and $z = 3.0$. *SMHM relation 3*: derived by Kravtsov (2013) for all galaxies only at $z = 0$. *SMHM relation 4*: derived by Rodríguez-Puebla et al. (2015) separately for blue and red galaxies only at $z = 0$. Note that there are significant differences among these SMHM relations, but because halo size depends weakly on halo mass ($R_{200c} \propto M_{200c}^{1/3}$), our main results are not sensitive to these differences.

width 0.15 dex are plotted as squares (error bars); only the bins with more than 5 galaxies are shown. The halo radius limit corresponding to the reference stellar masses $M_{*,\text{low}}$ in Table 1 are shown as a heavy tick mark at the bottom of each panel. The coefficient of proportionality α in the relation $R_{\text{eff}} = \alpha R_{200c}$ is nearly the same in all four cases; the median values of α are 0.021, 0.025, 0.023, and 0.024 for SMHM relations 1–4, respectively. These $R_{\text{eff}}-R_{200c}$ relations are approximately linear, but with some subtle differences depending on the adopted SMHM relation.

Kravtsov (2013) also found a linear relation, using completely independent samples of galaxies at $z = 0$ and deprojected 3D half-mass radii $R_{1/2}$ rather than the projected 2D half-light radii R_{eff} . The solid line in Figure 5 shows his derived relation $R_{1/2} = \alpha' R_{200c}$ with $\alpha' = 0.015$, assuming $R_{\text{eff}} = R_{1/2}$ for pure-disk galaxies. The bulk of our sample by number lies above this relation by ~ 0.2 dex, agreeing better at the high- and low-mass ends. There are a number of

possible explanations for this offset, one of them being the difference between 2D half-light (effective) and 2D half-mass radii. Szomoru et al. (2013) noted that for the galaxies more massive than $5 \times 10^{10} M_{\odot}$ at $0 < z < 2.5$, rest-frame g band 2D half-light radii are on average $\sim 25\%$ larger than 2D half-mass radii (presumably due to the influence of bulges), which could account for ~ 0.1 dex of the offset. We will address other explanations below in discussing the difference between morphological types, de-projection effects, and the redshift evolution.

Our second main result is that the $R_{\text{eff}}-R_{200c}$ relations are offset for late-type and early-type galaxies. To separate morphological types, we split our sample in two different ways: (1) high- n (early-type) and low- n (late-type) subsamples, and (2) low-sSFR (early-type) and high-sSFR (late-type) subsamples. We only include the highest and lowest 20% of the sample in either n or sSFR in the hope that this procedure will isolate disk-dominated from spheroid-dominated galaxies. The resulting $R_{\text{eff}}-R_{200c}$ relations for different morphological types using all four SMHM relations are shown in Figures 6 and 7.

We see in both Figures 6 and 7 that different morphological types follow sequences roughly parallel to the $R_{\text{eff}} \propto R_{200c}$ line with an offset of ~ 0.2 dex at $0 < z < 0.5$. This result is relatively robust against SMHM relation and morphological classification method: early-type (high- n or low-sSFR) galaxies have smaller R_{eff} than late-type (low- n or high-sSFR) galaxies at the same halo masses. The effect persists even if we compare 3D half-light radii rather than 2D half-light radii R_{eff} , although with a smaller separation between the sequences. The parallel sequences of early- and late-type galaxies in the $R_{\text{eff}}-R_{200c}$ diagram is reminiscent of the parallel sequences of spheroid- and disk-dominated galaxies in the J/M vs. M diagram (Fall 1983; Romanowsky & Fall 2012; Fall & Romanowsky 2013). The latter is due to a combination of different sizes (by a factor of ~ 2) and different rotation velocities (also by a factor of $\sim 2-3$) of spheroid- and disk-dominated galaxies of the same stellar mass.

This helps explain why our overall relation in Figure 5 is higher than Kravtsov’s at intermediate masses. Our sample is dominated by late-type galaxies ($\sim 90\%$ have $n < 2.5$), while Kravtsov’s sample is dominated by early-type galaxies ($\sim 80\%$ by number). He noted that late-type galaxies are systematically larger in $R_{1/2}$ than early-type galaxies at intermediate stellar masses, which is where we see the largest offset between these sequences in Figure 5. The changing morphological mix as a function of mass also helps explain the apparent curvature of the overall relation in Figure 5, because early-type galaxies dominate the high- and low-mass ends of the samples.

Our third main result is that the $R_{\text{eff}}-R_{200c}$ relation for late-type galaxies is close to the predictions of the simple analytic model of disk formation. The scale radius and effective radius of an exponential disk embedded in a dark-matter halo with a virial (outer) radius R_{200c} and a spin parameter λ are given by

$$R_d = \frac{\lambda}{\sqrt{2}} R_{200c} \quad (2)$$

and

$$R_{\text{eff}} = 1.68 R_d, \quad (3)$$

when the disk and halo have the same specific angular momentum (J/M). Equation (2) is exact for isothermal halos (Fall & Efstathiou 1980; see their Figure 3 and equation 42;

Fall 1983, see his equation 4) and is approximate for NFW halos with typical concentrations (Mo et al. 1998; Burkert et al. 2016). This prediction is shown as the dashed lines in Figures 6 to 9 for $\lambda = 0.035$, the peak of the universal spin parameter distribution (Bullock et al. 2001; Bett et al. 2007). We find that late-type galaxies at $0 < z < 0.5$ lie ~ 0.2 dex below the J/M equality line; in other words, our late-type galaxies have slightly less specific angular momentum than their dark-matter halos. This offset is consistent with direct measurements of specific angular momentum at $z = 0$, which indicate J/M retention factors $\eta_j \sim 80\% \pm 20\%$ for galactic disks (Fall & Romanowsky 2013).

Our fourth main result is that there is very little evolution in the $R_{\text{eff}}-R_{200c}$ relation from $z = 3$ to $z = 0$. This is shown in Figures 8 and 9. As in the previous diagrams, we select the highest and lowest 20% tails of the n and sSFR distributions. We only show results for SMHM relation 1, but we have checked that they are similar for the other SMHM relations. Figures 8 and 9 show again that in all redshift bins, late-type galaxies follow a linear relation: $R_{\text{eff}} = \alpha R_{200c}$. At $1 < z < 3$, late-type galaxies have $\alpha \approx 0.034$ in Figure 8 ($\alpha \approx 0.029$ in Figure 9) and lie close to the J/M equality line (within $\lesssim 0.1-0.2$ dex) with no discernable evolution. (There is a slight offset to smaller sizes in the late-type sample when selected by sSFR rather than Sérsic index.) This result agrees with recent direct measurements of specific angular momentum at $0.2 < z < 1.4$ (Contini et al. 2016) and at $1 < z < 3$ (Burkert et al. 2016), which show that J/M in galactic disks is nearly the same as in their dark-matter halos.

Kravtsov (2013) speculated that the sizes of galaxies grew in proportion to the sizes of their halos until $z \sim 2$ and then stopped, while their halos continued to grow in mass and size. While we see signs of evolution between our lowest redshift bins, both at $z < 1$, the relation for disks seems not to evolve at $z > 1$. This does not appear consistent with Kravtsov’s speculation. We believe we are seeing a real trend in the data at $z < 1$ that will require a different physical interpretation.

The interpretation for the relation of early-type galaxies is more uncertain. We see in Figures 8 and 9 that the trend for early type galaxies at all redshifts roughly parallels that for late-type galaxies, but shifted down by ~ 0.2 dex at $0 < z < 0.5$ and by $\sim 0.2-0.3$ dex at $0.5 < z < 3$. There is a slight hint of a “turnover” at the most massive end at $0 < z < 0.5$, but it is only apparent in the results using SMHM relation 2. The turnover, if real, could be due to either size-measurement biases (due to diffuse outer halos surrounding central galaxies in groups and clusters) or the breakdown of abundance matching for the group- or cluster-mass halos.

5. UNCERTAINTIES

How robust are these results? The uncertainties in this study potentially include measurement and statistical errors internal to the CANDELS dataset as well as external systematic errors from the adopted SMHM relations and stellar population models. Here we provide a brief assessment of these uncertainties.

As noted in Section 2, errors in the measurements of effective radii R_{eff} (from fits to Sérsic profiles) are relatively small: $< 20\%$ (systematic) to 30% (random). Even if these errors were at the upper end of this range for all galaxies and varied systematically with galactic masses and sizes, they would have a negligible influence on the coefficient and exponent of the galaxy size-halo size relation: $R_{\text{eff}} = \alpha R_{200c}^{\beta}$ with $|\Delta\alpha/\alpha| \lesssim 0.02$ and $|\Delta\beta| \lesssim 0.08$ (assuming a $\sim 20\%$

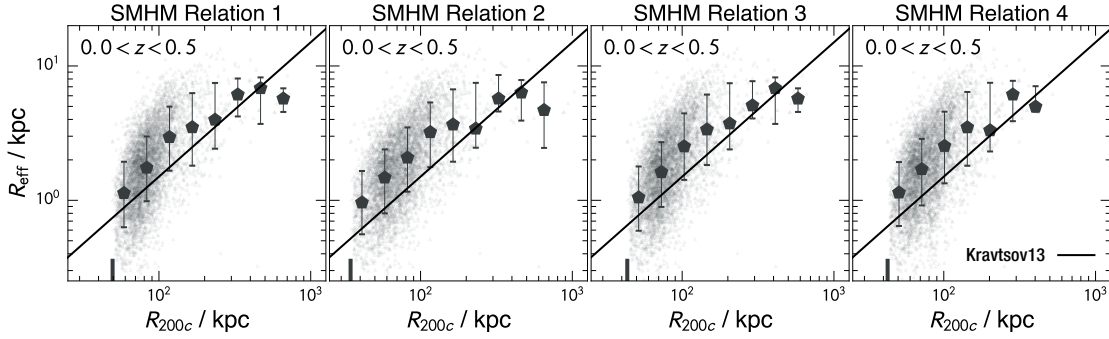


FIG. 5.— Galaxy effective radius R_{eff} plotted against halo virial radius R_{200c} in the lowest redshift interval ($0 < z < 0.5$) for the full sample of galaxies. The four panels show results for SMHM relations 1, 2, 3, and 4 as indicated. The tiny gray dots represent individual galaxies, while the filled pentagons and vertical bars indicate the median values and 16–84 percentile ranges of R_{eff} in bins of width 0.15 in $\log R_{200c}$. The diagonal lines show the $R_{1/2}$ – R_{200c} relation at $z = 0$ from Kravtsov (2013) assuming $R_{\text{eff}} = R_{1/2}$. The heavy tick mark at the bottom of each panel indicates the halo mass corresponding to the reference stellar mass $M_{*,\text{low}}$ listed in Table 1. Note that the R_{eff} – R_{200c} relations are similar for the four different SMHM relations and are roughly consistent with Kravtsov’s results. The R_{eff} – R_{200c} relations are linear in a first approximation but exhibit some curvature at high and low masses as a result of the changing mix of galaxy morphologies. Compare with Figures 6 and 7.

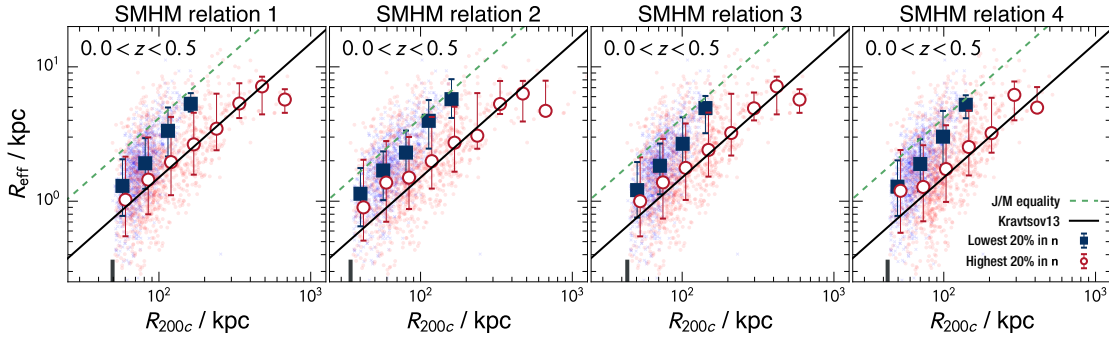


FIG. 6.— Galaxy effective radius R_{eff} plotted against halo virial radius R_{200c} in the lowest redshift interval ($0 < z < 0.5$) for subsamples of galaxies with the lowest and highest 20% of the measured Sérsic index n as proxies for late- and early-type galaxies, respectively. The four panels show results for SMHM relations 1, 2, 3, and 4 as indicated. The tiny blue and red dots represent individual low- n and high- n galaxies, respectively, while the filled blue squares, open red circles, and vertical bars indicate the corresponding median values and 16–84 percentile ranges of R_{eff} in bins of width 0.15 in $\log R_{200c}$. The diagonal solid lines show the $R_{1/2}$ – R_{200c} relation at $z = 0$ from Kravtsov (2013) assuming $R_{\text{eff}} = R_{1/2}$, while the diagonal dashed lines show the prediction for galactic disks with the same J/M as their surrounding halos. The heavy tick mark at the bottom of each panel indicates the halo mass corresponding to the reference stellar mass $M_{*,\text{low}}$ listed in Table 1. Note that the R_{eff} – R_{200c} relation for low- n galaxies is systematically above, and roughly parallel to, the relation for high- n galaxies. The R_{eff} – R_{200c} relations for both subsamples of galaxies are more linear than the relations for the full sample. Compare with Figures 5 and 7.

or smaller systematic deviation in R_{eff} for a factor of 10 or more variation in R_{200c}). Because the sample size in this study is so large ($N \sim 38000$), the effects of random errors in the size measurements on the mean R_{eff} – R_{200c} relations are even smaller. In a situation like this, with negligible internal errors, formal tests of goodness-of-fit are not informative, and we do not attempt them.

The dominant uncertainties in our galaxy size–halo size relations are most likely caused by possible systematic errors in our adopted SMHM relations. We can judge the magnitude of these errors by comparing the R_{eff} – R_{200c} relations plotted in Figures 5 to 7 for the four different SMHM relations. This comparison indicates that the SMHM relation may be responsible for systematic errors at the level ~ 0.1 – 0.2 dex, perhaps a little less for the combined sample of galaxies, perhaps a little more for the subsamples split by morphological type. Quantitative measures of the deviations among the R_{eff} – R_{200c} relations at $0 < z < 0.5$ confirm these impressions.

The contribution to the error budget from the adopted stellar population models, which determine the stellar masses and specific star formation rates, are smaller than those from the adopted SMHM relations. Systematic errors in stellar masses could affect the R_{eff} – R_{200c} relations at about the same level as

systematic errors in R_{eff} . The classification of the 3D shapes of galaxies (i.e., flat disks vs. round spheroids) by Sérsic index is highly problematic, because it is based only on the radial decline of the projected 2D surface brightness profiles. Nevertheless, the R_{eff} – R_{200c} relations we obtain from subsamples split by Sérsic index agree at the $\lesssim 0.1$ dex level with those from subsamples split by specific star formation rate.

Based on this assessment of uncertainties, most of the results of this paper appear to be robust. In particular, there is a strong, approximately linear correlation between the sizes of galaxies and their dark-matter halos over the full range of redshifts examined here, $0 < z < 3$. The coefficient of proportionality is larger for late-type galaxies than for early-type galaxies, which follow roughly parallel sequences, except possibly at the highest redshifts. For late-type galaxies, the observed R_{eff} – R_{200c} relation is generally consistent with simple models in which galactic disks grow with the same specific angular momentum as their dark-matter halos. There is some evidence for a slow-down in disk growth after $z \sim 1$, but the apparent deviation from the J/M equality line at $0 < z < 1$ is only ~ 0.2 dex and is therefore a marginal rather than a robust detection.

We have plotted and examined the R_{eff} – R_{200c} relations at all redshifts ($0 < z < 3$) for all four SMHM relations to determine

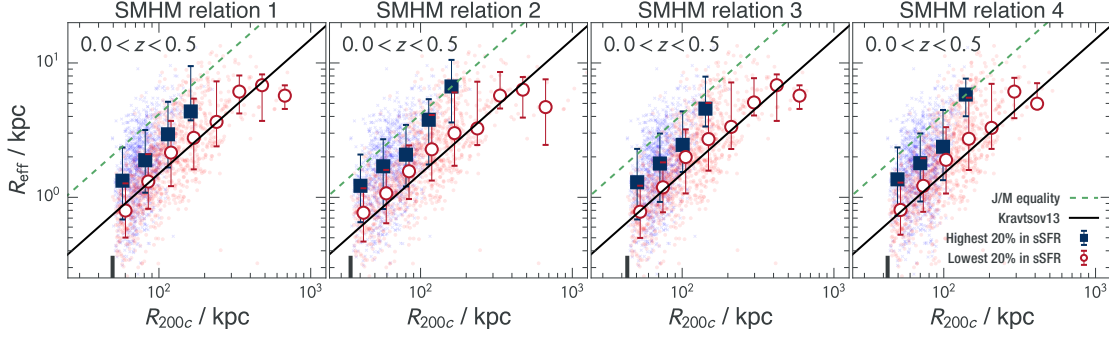


FIG. 7.— Galaxy effective radius R_{eff} plotted against halo virial radius R_{200c} in the lowest redshift interval ($0 < z < 0.5$) for subsamples of galaxies with the highest and lowest 20% of the measured specific star formation rate as proxies for late- and early-type galaxies, respectively. The four panels show results for SMHM relations 1, 2, 3, and 4 as indicated. The tiny blue and red dots represent individual high-sSFR and low-sSFR galaxies, respectively, while the filled blue squares, open red circles, and vertical bars indicate the corresponding median values and 16–84 percentile ranges of R_{eff} in bins of width 0.15 in $\log R_{200c}$. The diagonal solid lines show the $R_{1/2}$ – R_{200c} relation at $z = 0$ from Kravtsov (2013) assuming $R_{\text{eff}} = R_{1/2}$, while the diagonal dashed lines show the prediction for galactic disks with the same J/M as their surrounding halos. The heavy tick mark at the bottom of each panel indicates the halo mass corresponding to the reference stellar mass $M_{*,\text{low}}$ listed in Table 1. Note that the R_{eff} – R_{200c} relation for high-sSFR galaxies is systematically above, and roughly parallel to, the relation for low-sSFR galaxies. The R_{eff} – R_{200c} relations for both subsamples of galaxies are more linear than the relations for the full sample. Compare with Figures 5 and 6.

TABLE 2
VERIFICATION OF MAIN RESULTS

	SMHM 1	SMHM 2	SMHM 3	SMHM 4
1. The R_{eff} – R_{200c} relations are roughly linear in all redshift bins.	T	T	T	T
2. The R_{eff} – R_{200c} relations are offset for early- and late-type galaxies.	T	T	T	T
3. The R_{eff} – R_{200c} relation for late-type galaxies are close to the J/M equality line.	T	T	T	T
4. The R_{eff} – R_{200c} relation shows little evolution between $z = 0$ and $z = 3$.	T	T	T	T

whether or not they support the four main results discussed in Section 4. The outcome of this test is recorded in Table 2 by a T (for true) or F (for false) for each combination of SMHM relation and result. All of the entries are Ts. Table 2 therefore reinforces our conclusion that the main scientific results of this study are robust relative to discrepancies among the SMHM relations (because of the weak dependence of R_{200c} on M_{200c}).

6. DISCUSSION

We have found that the sizes of galaxies are proportional on average to the sizes of their dark-matter halos over a wide range of galaxy and halo masses and over the entire redshift range $0 < z < 3$ studied here: $R_{\text{eff}} = \alpha R_{200c}$ with $\alpha \approx 0.03$. In particular, we confirm the basic relation found by Kravtsov (2013) at $z = 0$ with only minor adjustment, some of which is related to the difference between 2D half-light radii and 3D half-mass radii. There is some curvature at the upper end of our overall R_{eff} – R_{200c} relation, which is due to the larger abundance and smaller average size of early-type galaxies compared with late-type galaxies of the same stellar mass. Indeed, we find that early- and late-type galaxies follow distinct, roughly parallel R_{eff} – R_{200c} relations offset by a factor of ~ 2 for the upper and lower 20 percentiles of Sérsic index and specific star formation rate, which are meant to be proxies for disk-dominated and spheroid-dominated galaxies.

Given the proportionality between galaxy and halo sizes, it is now straightforward to predict how galaxy sizes evolve with redshift, from the following alternative forms of equation (1):

$$R_{\text{eff}} = \alpha R_{200c} = \alpha \left[\frac{GM_{200c}}{100H^2(z)} \right]^{1/3} = \alpha \frac{V_{200c}}{10H(z)}. \quad (4)$$

Here, $H(z)$ is the Hubble parameter at redshift z , and V_{200c} is the circular velocity of the halo in question (see Mo et al. 1998). Thus, we expect $R_{\text{eff}} \propto H^{-2/3}(z)$ or $R_{\text{eff}} \propto H^{-1}(z)$ depending on whether galaxies at different z are compared at the same M_{200c} or V_{200c} . As a result of gravitational clustering, the characteristic halo mass evolves with redshift roughly as $\sigma(M_{200c}^*, z) \propto \delta_c(z)/D(z)$, where $\sigma(M_{200c}^*, z)$ is the RMS deviation of the linear density field smoothed over the scale $R(M_{200c}^*)$, $\delta_c(z)$ is the critical linear overdensity for collapse (Kitayama & Suto 1996), and $D(z)$ is the linear growth factor (Carroll et al. 1992). The corresponding galactic size $R_{\text{eff}}^*(z)$ at the knee of the galaxy mass function should evolve according to equation (4) with $M_{200c} \rightarrow M_{200c}^*(z)$. This expression for $R_{\text{eff}}^*(z)$ relates the typical sizes of progenitor–descendant pairs of galaxies at different redshifts, although there will be a large dispersion about it as a result of stochasticity in the hierarchical growth of galaxies.

Our R_{eff} – R_{200c} relations for late-type galaxies (defined by low n , high sSFR) at $1 < z < 3$ are within $\lesssim 0.1$ – 0.2 dex of the predictions of simple models in which galactic disks acquire and retain the same specific angular momentum as induced by tidal torques in their surrounding dark-matter halos. At $0 < z < 1$, late-type galaxies are ~ 0.2 dex below this prediction. However, given possible systematic errors in the measurements of galactic sizes ($\lesssim 20\%$ for low- n galaxies), our results are consistent with a range $\eta_j \sim 80\% \pm 20\%$ for the retained fraction of specific angular momentum. Our results therefore agree nicely with recent, direct measurements of the specific angular momentum of galactic disks at $z = 0$ (Fall & Romanowsky 2013), at $0.2 < z < 1.4$ (Contini et al. 2016), and at $1 < z < 3$ (Burkert et al. 2016), all of which indicate retention factors η_j near unity or slightly below.

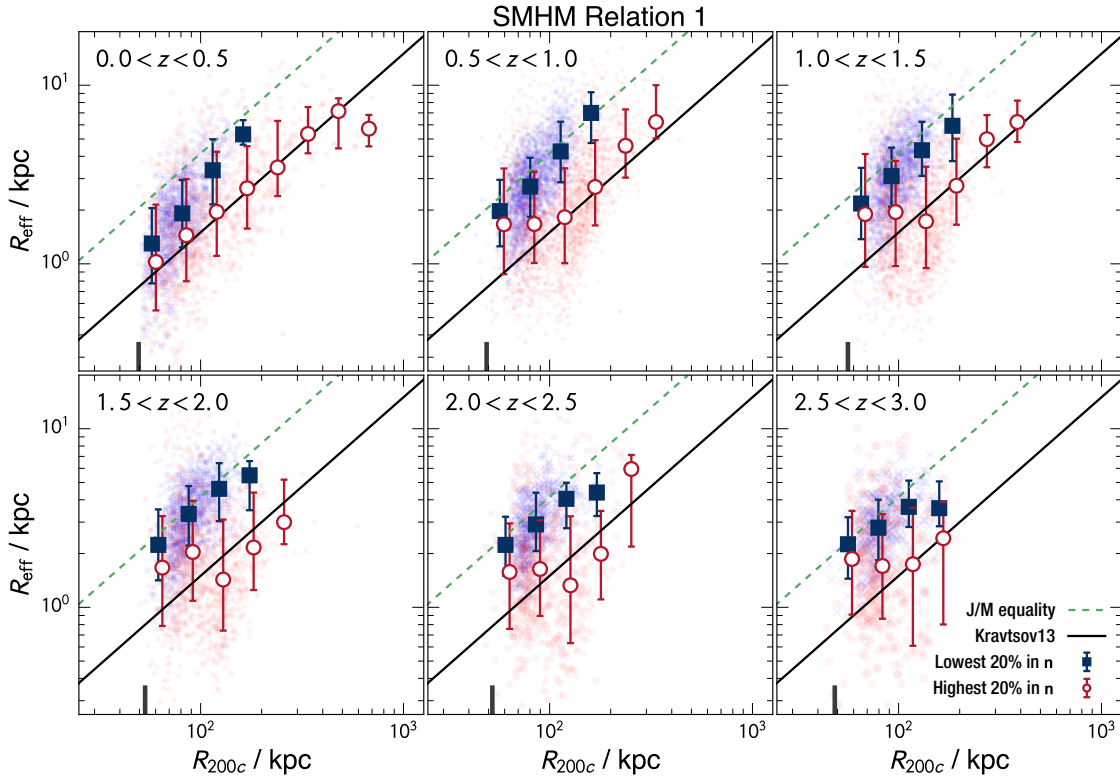


FIG. 8.— Galaxy effective radius R_{eff} plotted against halo virial radius R_{200c} at different redshifts for subsamples of galaxies with the lowest and highest 20% of the measured Sérsic index n as proxies for late- and early-type galaxies, respectively. The six panels show results computed from SMHM relation 1 in redshift intervals of $\Delta z = 0.5$ covering the range $0 < z < 3$. The faded blue and red symbols represent individual low- n and high- n galaxies, respectively, while the filled blue squares, open red circles, and vertical bars indicate the corresponding median values and 16–84 percentile ranges of R_{eff} in bins of width 0.15 in $\log R_{200c}$. The diagonal solid lines show the $R_{1/2}$ – R_{200c} relation at $z = 0$ from Kravtsov (2013) assuming $R_{\text{eff}} = R_{1/2}$, while the diagonal dashed lines show the prediction for galactic disks with the same J/M as their surrounding halos. The heavy tick mark at the bottom of each panel indicates the halo mass corresponding to the reference stellar mass $M_{*,\text{low}}$ listed in Table 1. Note that the R_{eff} – R_{200c} relations for both low- n and high- n galaxies are nearly constant with redshift, and that the one-to-one relation of angular momentum conservation is fit in disks and in rough balance, leading to an apparent (if not strict)

conservation of angular momentum during the formation of galactic disks. Simulations and now observations indicate that galaxies of all types grow in a quasi-homologous (or self-similar) relationship with their dark-matter halos. The details of how this happens are a topic of ongoing research.

The notion of angular momentum conservation was introduced as a simplifying approximation in the era of analytical models of galaxy formation (Fall & Efstathiou 1980). Since then, hydrodynamical models have revealed a much more complex situation. In particular, it is now clear that several physical processes may change the specific angular momentum of galaxies or parts of galaxies during their formation and evolution, including merging, feedback, inflows, outflows, and gravitational interactions between baryons and dark matter. Some of these processes cause gains in specific angular momentum, while others cause losses (see Romanowsky & Fall 2012 and Genel et al. 2015 for summaries and references to earlier work).

The galactic disks that form in recent hydrodynamical simulations have nearly the same specific angular momentum on average as their dark-matter halos, in good agreement with observations (Genel et al. 2015; Pedrosa & Tissera 2015; Teklu et al. 2015; Zavala et al. 2016). Evidently, the processes responsible for gains and losses are either weak

We thank Gerard Lemson for the help with Millennium Simulation, Adam Tomczak for useful discussions of stellar mass functions, and Andrey Kravtsov for providing conversion factors between different halo mass definitions. We also thank Avishai Dekel, Sandra Faber, Steve Finkelstein, Andrey Kravtsov, Yu Lu, and Rachel Somerville for comments on a near-final draft of this paper. This work is based on observations taken by the CANDELS Multi-Cycle Treasury Program with the NASA/ESA HST, which is operated by the Association of Universities for Research in Astronomy, Inc., under NASA contract NAS5-26555.

APPENDIX

TRANSFORMATION BETWEEN THE $R_{\text{eff}}-M_*$ AND $R_{\text{eff}}-R_{200c}$ RELATIONS

The halo virial radius R_{200c} of each galaxy in our sample was computed by the abundance-matching technique, i.e., from its stellar mass M_* , the SMHM relation, and Equation (1). Thus, the positions of galaxies in the $R_{\text{eff}}-R_{200c}$ plane represent a non-linear transformation of their positions in the $R_{\text{eff}}-M_*$ plane. While the former is more fundamental from a theoretical perspective,

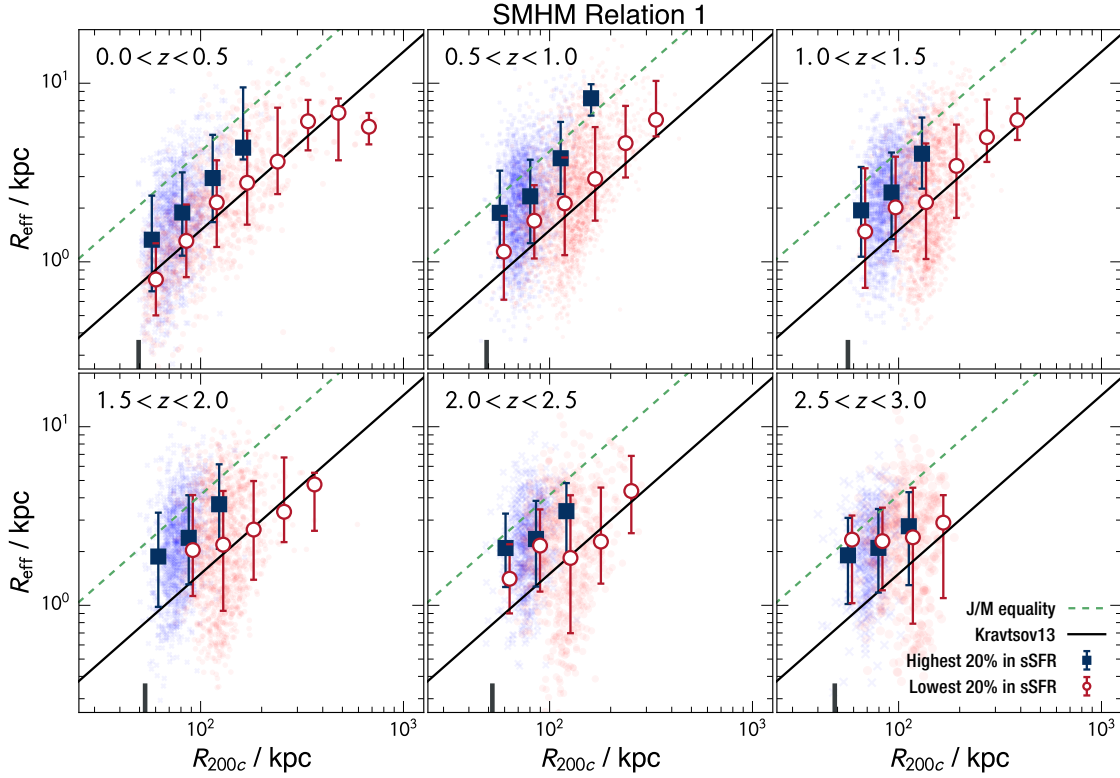


FIG. 9.— Galaxy effective radius R_{eff} plotted against halo virial radius R_{200c} at different redshifts for subsamples of galaxies with the highest and lowest 20% of the measured specific star formation rate as proxies for late- and early-type galaxies, respectively. The six panels show results computed from SMHM relation 1 in redshift intervals of $\Delta z = 0.5$ covering the range $0 < z < 3$. The faded blue and red symbols represent individual high-sSFR and low-sSFR galaxies, respectively, while the filled blue squares, open red circles, and vertical bars indicate the corresponding median values and 16–84 percentile ranges of R_{eff} in bins of width 0.15 in $\log R_{200c}$. The diagonal solid lines show the $R_{1/2}$ – R_{200c} relation at $z = 0$ from Kravtsov (2013) assuming $R_{\text{eff}} = R_{1/2}$, while the diagonal dashed lines show the prediction for galactic disks with the same J/M as their surrounding halos. The heavy tick mark at the bottom of each panel indicates the halo mass corresponding to the reference stellar mass $M_{*,\text{low}}$ listed in Table 1. Note that the R_{eff} – R_{200c} relations for both high-sSFR and low-sSFR galaxies are nearly constant with redshift, and that the one for high-sSFR galaxies is close to the predicted relation for equality of J/M in disks and halos. Compare with Figure 8.

and is the main focus of this paper, the latter is one step closer to the observations, since it requires only the conversion of luminosities and colors into stellar masses. It is therefore of interest to examine the R_{eff} – M_* diagrams for our sample and how they map into the R_{eff} – R_{200c} diagrams presented in Section 4. This is the purpose of this appendix.

Figure 10 shows the R_{eff} – M_* diagram for galaxies in our sample in six redshift intervals covering the range $0 < z < 3$ when divided, as before, into subsamples with the lowest and highest quintiles of Sérsic index n . We also plot in this diagram the median values of R_{eff} in bins of width 0.5 in $\log M_*$ for these two subsamples. Evidently, the median R_{eff} – M_* relation for low- n galaxies is close to a single power law (a straight line in a plot of $\log R_{\text{eff}}$ against $\log M_*$), whereas the relation for high- n galaxies is more complicated; it is flatter than the low- n relation at low masses and steeper at high masses, with a bend at $M_* \sim \text{few} \times 10^{10} M_\odot$. It is also clear from Figure 10 that the median R_{eff} – M_* relations for both low- n and high- n galaxies evolve very slowly. For subsamples with the highest and lowest quintiles of specific star formation rate, we find similar behaviors in the median R_{eff} – M_* relations, as functions of both M_* and z , especially for $z < 1.5$ (not shown here).

Figure ?? shows the result of transforming the R_{eff} – M_* diagram into the R_{eff} – R_{200c} diagram with SMHM relation 1. This is exactly the same as Figure 8 except that we have omitted the vertical bars for clarity. We have already discussed this diagram at length in Section 4. Here we note only that the median R_{eff} – R_{200c} relations for low- n and high- n galaxies in Figure ?? appear more parallel than the corresponding R_{eff} – M_* relations in Figure 10, particularly at $z < 1.5$, where they are best defined. This is a consequence of the non-linearity of the SMHM relation, especially near $M_{200c} \sim 10^{12} M_\odot$, corresponding to $M_* \sim \text{few} \times 10^{10} M_\odot$, and hence near the bend in the R_{eff} – M_* relation for high- n galaxies.

van der Wel et al. (2014) also derived R_{eff} – M_* relations in the redshift range $0 < z < 3$ for galaxies in the CANDELS sample. The main difference between their work and ours is that they adopted the same selection limits in all CANDELS regions, whereas we adopted fainter selection limits in the Deep and HUDF regions. As a result, our R_{eff} – M_* relations extend to much lower M_* than theirs. Otherwise, the selection of galaxies and measurement of their properties are nearly identical in the two studies. van der Wel et al. (2014) divided their sample into blue and red galaxies on the basis of rest-frame UVJ colors rather than by Sérsic

index or specific star formation rate, as we have done. Naturally, there is a general, but not a perfect, correspondence between these three different proxies for late- and early-type galaxies.

van der Wel et al. (2014) fitted power laws to the $R_{\text{eff}}-M_*$ relations for blue and red galaxies; these are shown in Figure 10 as the blue solid and red dashed line segments, respectively. For red galaxies, they truncated the fits at $M_* = 2 \times 10^{10} M_\odot$ because they also noticed a bend in the $R_{\text{eff}}-M_*$ relation near this mass and a flattening below it. We obtain nearly identical results when we divide our sample into blue and red galaxies using the same cuts in rest-frame UVJ colors as van der Wel et al. (2014). The blue solid and red dashed curves in Figure ?? show how the van der Wel et al. (2014) power laws in the $R_{\text{eff}}-M_*$ diagram transform into the $R_{\text{eff}}-R_{200c}$ diagram. As expected, this mapping introduces curvature and makes the $R_{\text{eff}}-R_{200c}$ relations for blue and red galaxies somewhat more parallel. However, the transformed relations cover only a narrow range of halo sizes, roughly $100 \text{ kpc} \lesssim R_{200c} \lesssim 300 \text{ kpc}$, except in the lowest redshift interval. We have been able to extend the $R_{\text{eff}}-R_{200c}$ relations to a wider range of halo sizes, roughly $50 \text{ kpc} \lesssim R_{200c} \lesssim 300 \text{ kpc}$, with our fainter selection limits in the CANDELS Deep and HUDF regions.

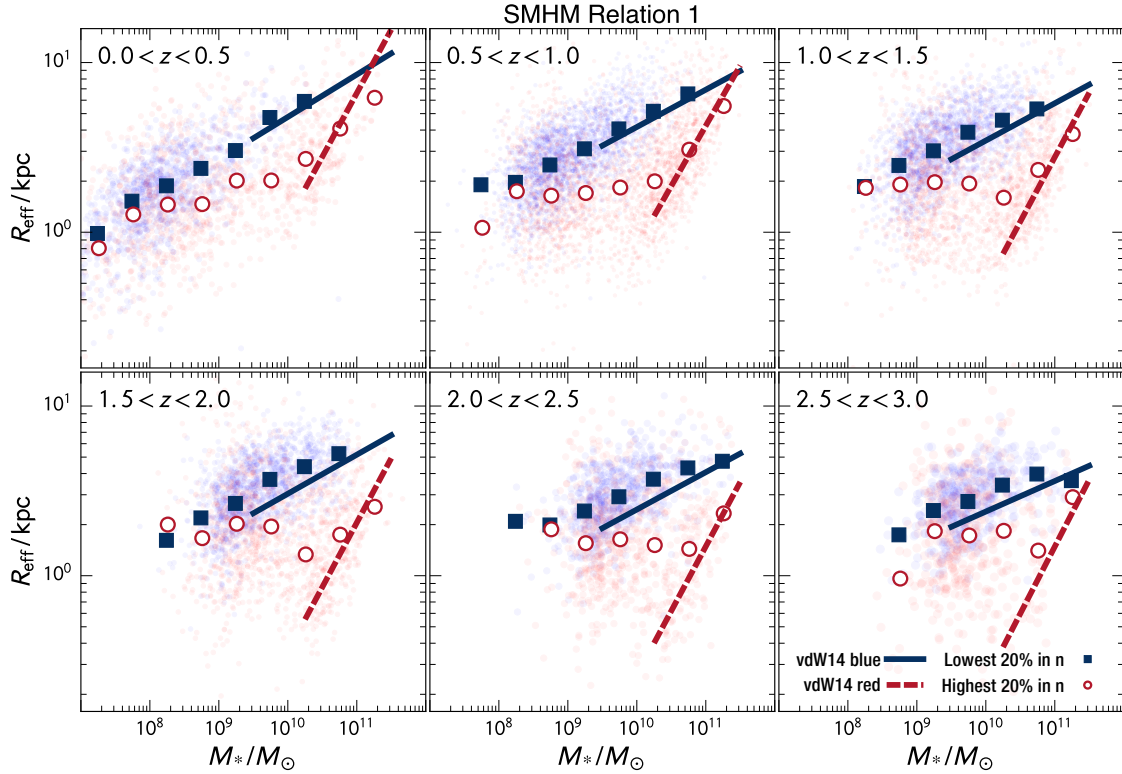


FIG. 10.— Galaxy effective radius R_{eff} plotted against stellar mass M_* at different redshifts for subsamples of galaxies with the lowest and highest 20% of the measured Sérsic index n as proxies for late- and early-type galaxies, respectively. The six panels show results computed from SMHM relation 1 in redshift intervals of $\Delta z = 0.5$ covering the range $0 < z < 3$. The faded blue and red symbols represent individual low- n and high- n galaxies, respectively, while the filled blue squares and open red circles indicate the corresponding median values of R_{eff} in bins of width 0.5 in $\log M_*$. The blue solid and red dashed lines show the power-law fits to the $R_{\text{eff}}-M_*$ relations for blue and red galaxies (defined in terms of rest-frame UVJ colors) from van der Wel et al. (2014). Note that our sample extends to fainter and therefore less massive galaxies than the van der Wel et al. (2014) sample. Compare with Figure ??.

REFERENCES

- Behroozi, P. S., Wechsler, R. H., & Conroy, C. 2013, *ApJ*, 770, 57
 Bertin, E., & Arnouts, S. 1996, *A&AS*, 117, 393
 Bett, P., Eke, V., Frenk, C. S., et al. 2007, *MNRAS*, 376, 215
 Boylan-Kolchin, M., Springel, V., White, S. D. M., Jenkins, A., & Lemson, G. 2009, *MNRAS*, 398, 1150
 Bouwens, R., Illingworth, G. D., Oesch, P. A., et al. 2010, *ApJ*, 709, L133
 Bouwens, R. J., Illingworth, G. D., Oesch, P. A., et al. 2010, *ApJ*, 709, L133
 Bryan, G. L., & Norman, M. L. 1998, *ApJ*, 495, 80
 Bullock, J. S., Dekel, A., Kolatt, T. S., et al. 2001, *ApJ*, 555, 240
 Burkert, A., Förster Schreiber, N. M., Genzel, R., et al. 2016, *ApJ*, 826, 214
 Carroll, S. M., Press, W. H., & Turner, E. L. 1992, *ARA&A*, 30, 499
 Chabrier, G. 2003, *PASP*, 115, 763
 Cole, S., Lacey, C. G., Baugh, C. M., & Frenk, C. S. 2000, *MNRAS*, 319, 168
 Contini, T., Epinat, B., Bouché, N., et al. 2016, *A&A*, 591, A49
 Croton, D. J., Stevens, A. R. H., Tonini, C., et al. 2016, *ApJS*, 222, 22
 Curtis-Lake, E., McLure, R. J., Dunlop, J. S., et al. 2016, *MNRAS*, 457, 440
 Diemer, B., More, S., & Kravtsov, A. V. 2013, *ApJ*, 766, 25
 Diemer, B., & Kravtsov, A. V. 2015, *ApJ*, 799, 108
 Dutton, A. A., Conroy, C., van den Bosch, F. C., Prada, F., & More, S. 2010, *MNRAS*, 407, 2
 Ellis, R. S., McLure, R. J., Dunlop, J. S., et al. 2013, *ApJ*, 763, L7

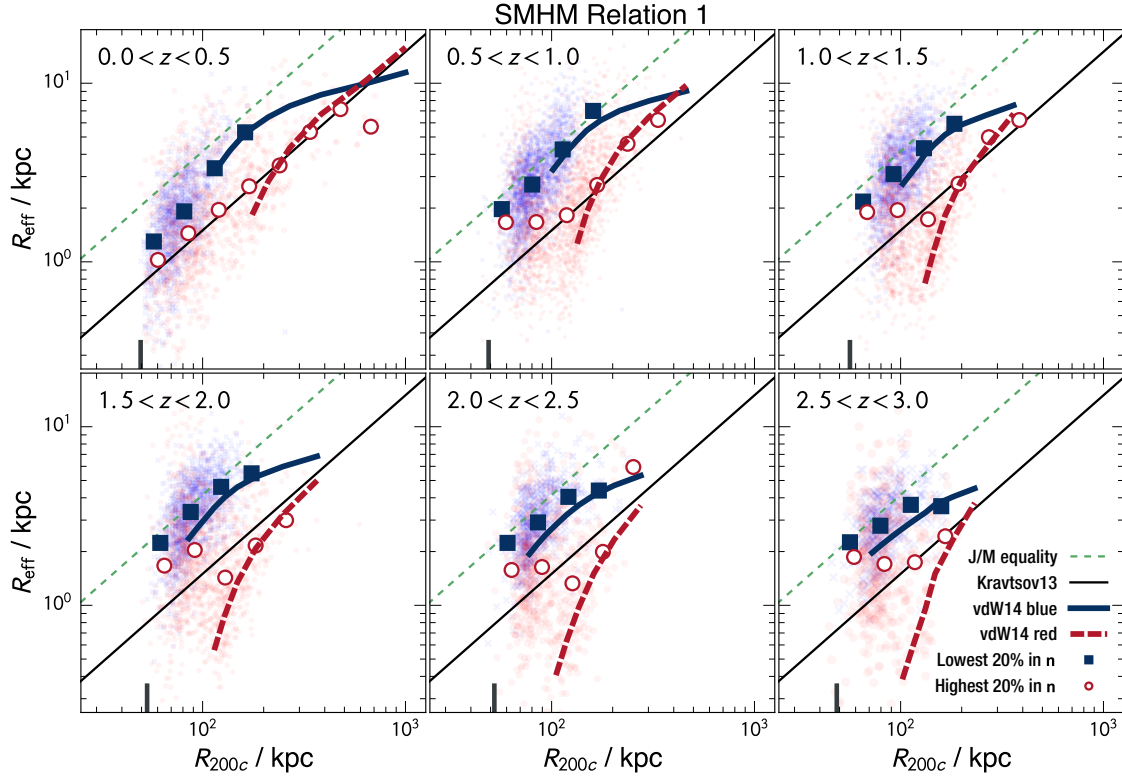


FIG. 11.— Galaxy effective radius R_{eff} plotted against halo virial radius R_{200c} at different redshifts for subsamples of galaxies with the lowest and highest 20% of the measured Sérsic index n as proxies for late- and early-type galaxies, respectively. The six panels show results computed from SMHM relation 1 in redshift intervals of $\Delta z = 0.5$ covering the range $0 < z < 3$. The faded blue and red symbols represent individual low- n and high- n galaxies, respectively, while the filled blue squares and open red circles indicate the corresponding median values of R_{eff} in bins of width 0.15 in $\log R_{200c}$. The diagonal solid lines show the $R_{1/2}$ – R_{200c} relation at $z = 0$ from Kravtsov (2013) assuming $R_{\text{eff}} = R_{1/2}$, while the diagonal dashed lines show the prediction for galactic disks with the same J/M as their surrounding halos. The heavy tick mark at the bottom of each panel indicates the halo mass corresponding to the reference stellar mass $M_{*,\text{low}}$ listed in Table 1. The blue solid and red dashed curves are the power-law fits for blue and red galaxies in the R_{eff} – M_* plane after transformation into the R_{eff} – R_{200c} plane. Compare with Figure 10.

Fall, S. M., & Efstathiou, G. 1980, MNRAS, 193, 189
 Fall, S. M. 1983, in IAU Symp. 100, Internal Kinematics and Dynamics of Galaxies, ed. E. Athanassoula (Cambridge: Cambridge Univ. Press), 391
 Fall, S. M., & Romanowsky, A. J. 2013, ApJ, 769, L26
 Ferguson, H. C., Dickinson, M., Giavalisco, M., et al. 2004, ApJ, 600, L107
 Galametz, A., Grazian, A., Fontana, A., et al. 2013, ApJS, 206, 10
 Genel, S., Fall, S. M., Hernquist, L., et al. 2015, ApJ, 804, L40
 Grogin, N. A., Kocevski, D. D., Faber, S. M., et al. 2011, ApJS, 197, 35
 Guo, Y., Ferguson, H. C., Giavalisco, M., et al. 2013, ApJS, 207, 24
 Hathi, N. P., Malhotra, S., & Rhoads, J. E. 2008, ApJ, 673, 686–693
 Huang, K.-H., Ferguson, H. C., Ravindranath, S., & Su, J. 2013, ApJ, 765, 68
 Hudson, M. J., Gillis, B. R., Coupon, J., et al. 2015, MNRAS, 447, 298
 Illingworth, G. D., Magee, D., Oesch, P. A., et al. 2013, ApJS, 209, 6
 Kitayama, T., & Suto, Y. 1996, ApJ, 469, 480
 Koekemoer, A. M., Faber, S. M., Ferguson, H. C., et al. 2011, ApJS, 197, 36
 Koekemoer, A. M., Ellis, R. S., McLure, R. J., et al. 2013, ApJS, 209, 3
 Kravtsov, A. V. 2013, ApJ, 764, L31
 Mandelbaum, R., Wang, W., Zu, Y., et al. 2016, MNRAS, 457, 3200
 Mo, H. J., Mao, S., & White, S. D. M. 1998, MNRAS, 295, 319
 Mobasher, B., Dahlen, T., Ferguson, H. C., et al. 2015, ApJ, 808, 101

Moustakas, J., Coil, A. L., Aird, J., et al. 2013, ApJ, 767, 50
 Mosleh, M., Williams, R. J., Franx, M., et al. 2012, ApJ, 756, L12
 Pedrosa, S. E., & Tissera, P. B. 2015, A&A, 584, A43
 Peng, C. Y., Ho, L. C., Impey, C. D., & Rix, H.-W. 2010, AJ, 139, 2097
 Rodríguez-Puebla, A., Avila-Reese, V., Yang, X., et al. 2015, ApJ, 799, 130
 Romanowsky, A. J., & Fall, S. M. 2012, ApJS, 203, 17
 Salmon, B., Papovich, C., Finkelstein, S. L., et al. 2015, ApJ, 799, 183
 Santini, P., Ferguson, H. C., Fontana, A., et al. 2015, ApJ, 801, 97
 Shibuya, T., Ouchi, M., & Harikane, Y. 2015, ApJS, 219, 15
 Straatman, C. M. S., Spitler, L. R., Quadri, R. F., et al. 2016, ApJ, 830, 51
 Szomoru, D., Franx, M., van Dokkum, P. G., et al. 2013, ApJ, 763, 73
 Taghizadeh-Popp, M., Fall, S. M., White, R. L., & Szalay, A. S. 2015, ApJ, 801, 14
 Teklu, A. F., Remus, R.-S., Dolag, K., et al. 2015, ApJ, 812, 29
 Tomczak, A. R., Quadri, R. F., Tran, K.-V. H., et al. 2014, ApJ, 783, 85
 van der Wel, A., Bell, E. F., Häussler, B., et al. 2012, ApJS, 203, 24
 van der Wel, A., Franx, M., van Dokkum, P. G., et al. 2014, ApJ, 788, 28
 Wechsler, R. H., Bullock, J. S., Primack, J. R., Kravtsov, A. V., & Dekel, A. 2002, ApJ, 568, 52
 Zavala, J., Frenk, C. S., Bower, R., et al. 2016, MNRAS, in press